

## Deuterium retention in tungsten fiber-reinforced tungsten composites

A. Kärcher<sup>a,b</sup>, J. Riesch<sup>a</sup>, P. Almanstötter<sup>a,c</sup>, A. Manhard<sup>a</sup>, M. Balden<sup>a</sup>, J.W. Coenen<sup>d,e</sup>,  
K. Hunger<sup>a</sup>, H. Maier<sup>a</sup>, L. Raumann<sup>d</sup>, D. Schwalenberg<sup>b,d</sup>, R. Neu<sup>a,b,\*</sup>

<sup>a</sup> Max-Planck-Institut für Plasmaphysik, Garching, Germany

<sup>b</sup> Technische Universität München, Garching, Germany

<sup>c</sup> Universität Augsburg, Augsburg, Germany

<sup>d</sup> Forschungszentrum Jülich, Institut für Energie & Klimaforschung, Jülich, Germany

<sup>e</sup> Department of Engineering Physics, University of Wisconsin Madison, Madison 53706, WI, USA

### ABSTRACT

In future fusion reactors, plasma-facing materials (PFMs) have to withstand unique conditions such as high temperatures, ion and neutron irradiation. Tungsten (W) has been established as main candidate material due to its favorable properties regarding the fusion environment but brings one major challenge: Its brittleness at moderate temperatures can lead to failure of tungsten components. Tungsten fiber-reinforced tungsten ( $W_f/W$ ), a tungsten matrix containing drawn tungsten fibers, was developed to mitigate this problem by using extrinsic toughening mechanisms to achieve pseudo-ductility. The deuterium (D) retention in  $W_f/W$  manufactured by chemical vapor deposition (CVD) has been investigated using  $W_f/W$  single layered model systems consisting of a single plane of unidirectional tungsten fibers embedded in a tungsten matrix produced by CVD. Various parameters with potential influence on the D retention, such as the choice of an erbium oxide interface and potassium doping, have been included in the investigation. The samples have been ground to varying distances between surface and fiber plane - exposing distinct details of the  $W_f/W$  microstructures at the surface. The samples were exposed to a low temperature D plasma at 370 K for 72 h resulting in a total fluence of  $10^{25}$  D/m<sup>2</sup>. The D retention of all samples was measured by nuclear reaction analysis (NRA) and thermal desorption spectroscopy (TDS). The D retention in  $W_f/W$  composites is higher than in reference samples made from hot-rolled W by factors between 2 and 5. In addition, a comparison of NRA and TDS data indicates that D penetrates faster into the depth of  $W_f/W$  material than into hot-rolled tungsten.

### 1. Introduction

Tungsten has emerged as the most promising armor material for the divertor in a future nuclear fusion reactor. Its very high melting point, high temperature strength and the low sputter yield enable high durability even under the extreme conditions present in this part of the reactor [1,2]. Especially the combination of low sputter yield together with its low vapor pressure prevents contamination of the plasma. The hydrogen retention of tungsten is small due to the lack of chemical bonds between hydrogen and tungsten, as well as the low solubility of hydrogen in tungsten [3].

However, tungsten is brittle at room temperature and prone to embrittlement by neutron irradiation or recrystallization and grain growth during operation [4]. As the material is cyclically strained by steep temperature gradients, cracks at the surface can ultimately lead to catastrophic failure of the plasma-facing components (PFCs).

To increase the fracture toughness, tungsten fiber-reinforced tungsten composites ( $W_f/W$ ) were developed for the use in the divertors of future fusion devices [5]. In these composites, drawn tungsten wire produced by

OSRAM GmbH [6] is used as fibrous reinforcements in a tungsten matrix. Between fiber and matrix, an engineered interface is used to enable extrinsic toughening mechanisms that can stop crack propagation through local energy dissipation. So far, two main fabrication approaches have been established: Powder metallurgical processes [7,8] and chemical vapor deposition [9–11]. For both approaches, the improvement of the mechanical properties has been shown [8,12].  $W_f/W$  manufactured by chemical vapor deposition is used for this study. A schematic drawing of this type of  $W_f/W$  and a metallographic cross section of the material can be seen in Fig. 1. The CVD  $W_f/W$  composites contain unidirectional tungsten fibers of 150  $\mu\text{m}$  diameter coated by an interface and embedded in a tungsten matrix. In preparation for the CVD process, the tungsten wire is wound onto a frame consisting of two fine threaded top ends and clamped down to form an even plane. After an interface layer is applied to the fibers, the whole frame is exposed to both  $\text{WF}_6$  and  $\text{H}_2$  gas under temperatures between 573 and 1073 K, preserving the initial state of the fibers. In order to achieve bulk material, further layers of fibers are added on top and embedded successively. For details please refer to [9–11].

\* Corresponding author at: Max-Planck-Institut für Plasmaphysik, Garching, Germany.

E-mail address: [rudolf.neu@ipp.mpg.de](mailto:rudolf.neu@ipp.mpg.de) (R. Neu).

<https://doi.org/10.1016/j.nme.2021.100972>

Received 18 August 2020; Received in revised form 16 February 2021; Accepted 10 March 2021

Available online 17 March 2021

2352-1791/© 2021 The Author(s).

Published by Elsevier Ltd.

This is an open access article under the CC BY-NC-ND license

(<http://creativecommons.org/licenses/by-nc-nd/4.0/>).

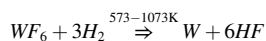
The fibers and the CVD matrix strongly influence the microstructure of the  $W_f/W$  composite: The grains of drawn tungsten fibers are severely deformed and elongated and the grains of the CVD matrix show a columnar growth starting at the fibers' surface. Due to this prominent microstructure and due to the incorporation of foreign materials as interface, the properties of  $W_f/W$  composites in the fusion environment potentially differ from the established properties of pure tungsten material. These aspects of the material have to be investigated and understood.

In this article, a study of the hydrogen (isotope) retention in  $W_f/W$  composites produced by chemical vapor deposition is presented. In order to enable the isolation of certain microstructural features within the material, single-layered model systems have been developed. The  $W_f/W$  model system consists of one layer of fibers that was suspended vertically during the CVD process and exposed to  $WF_6$  and  $H_2$  gas from both sides, ensuring an even growth of the tungsten matrix.

By grinding, microstructures of areas at different distances to the fiber plane are exposed on the surface and then exposed to deuterium (D) plasma. The retained D is then measured in the near-surface volume by nuclear reaction analysis (NRA) and in the whole volume of the sample by thermal desorption spectroscopy (TDS).

## 2. The material

Chemical vapor deposition of tungsten uses the chemical reaction:



$WF_6$  is reduced by  $H_2$  in a surface reaction when subjected to temperatures above 573 K and the tungsten can then adhere to the exposed surface. The vessel is flushed with  $H_2$  before the deposition in order to obtain steady temperatures at the beginning of the deposition.

The gas flow during the CVD process was constant for all CVD  $W_f/W$  plates produced for this study: The  $WF_6$  gas at 400 sccm and the  $H_2$  gas at 2010 sccm. Some parameters were moderately varied in an effort for process optimization, as shown in Table 1.

Differences of temperature during the CVD procedure lead to different growth rates with respect to the matrix, which potentially influences its microstructural properties. As can be seen in Table 1, the estimated fiber temperature and the heater temperature varied slightly between different depositions. The duration of exposure to  $H_2$  gas before the chemical vapor deposition was reduced for the plates "c" and "d" as the impact of the temperature variations at the beginning of deposition

were deemed to be negligible compared to the entire deposition.

Two fiber-to-fiber distances are realized in the CVD  $W_f/W$  model system samples. The distance of 250  $\mu m$  from one fiber center to the next is the typical fiber distance used in multi-layer  $W_f/W$  mockups as described in [9]. The spacing between the fibers is 100  $\mu m$ . Additionally, the fiber-to-fiber distance of 500  $\mu m$ , with a spacing between the fibers of 350  $\mu m$ , is chosen in order to resolve the influence of the fiber-matrix structure on D retention in lateral NRA scans.

As the influence of fiber coating on the D retention of the material is also of interest, samples with and without an erbium oxide interface coating on the fibers are studied. The oxide interface used in this study is an approximately 1  $\mu m$  thick and was produced by reactive magnetron sputtering using a radio frequency with the power of 450 W. As deposition process atmosphere, 40 sccm Ar and 8 sccm  $O_2$  are used. The frame is placed in the deposition chamber and coated for 210 min and then turned around to coat the other side for the same amount of time [13,14].

In addition, some samples (denoted in Table 2) contain fibers doped with potassium (K). Since K has a low solubility in tungsten, it gathers at grain boundaries preventing grain growth. This effect is used to preserve the microstructure and therefore the ductile behavior of tungsten fibers at high temperatures [15].

The reference material used for this study is hot-rolled tungsten produced by PLANSEE AG. During the production process, tungsten powder is pressed and sintered into blocks. These blocks are then worked with a hot rolling mill and ground to a plane-parallel finish, producing tungsten sheets with a thickness of 0.8 mm. The sheets are then cut into 10  $\times$  10 mm sample plates. This material has previously been characterized thoroughly in [16]. The tungsten samples are named 1-Wref and 2-Wref.

### 2.1. Sample preparation

The samples are each ground to specific fiber configurations that are characterized by the distance of the fibers to the upper surface of the sample and are revealing different microstructures at the surface.

In total, four configurations are chosen, as seen in Fig. 2:

- All fibers are aimed to be cut in half for this configuration in the effort to expose as much fiber material as possible on the surface to observe their influence on H retention. A "half-cut" sample has a high surface fraction of fibers. As the near-surface area is then strongly affected by fibers, the influence of the fibers can be

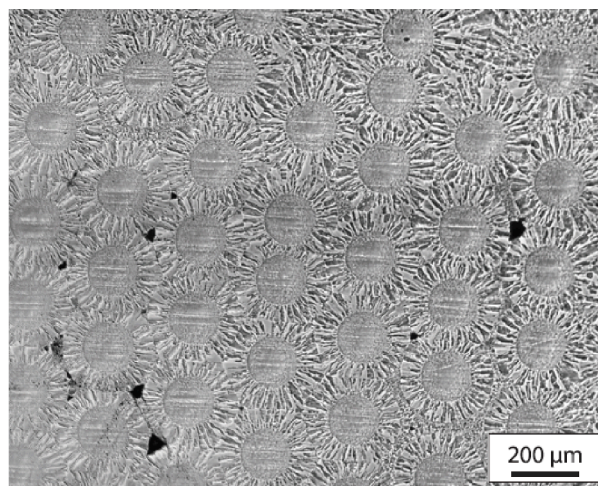
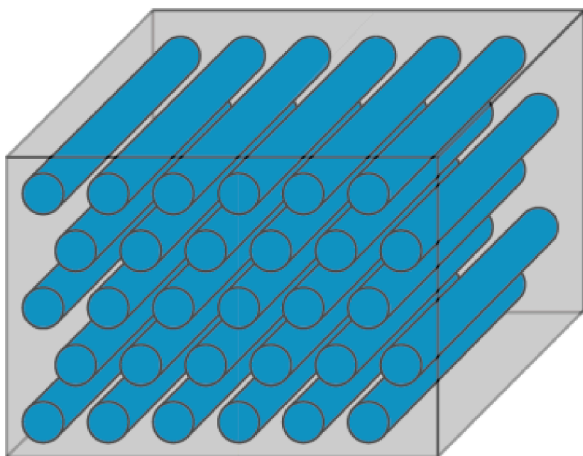


Fig. 1. Schematic drawing of a bulk CVD  $W_f/W$  composite (left) and a metallographic cross section (right) [18]. The schematic drawing (left) shows the drawn tungsten fibers (blue) that are embedded in a tungsten matrix (grey). The metallographic cross section shows the distribution of fibers (round shapes), the CVD tungsten matrix, which is grown on the fibers, and pores (black).

**Table 1**Parameters for the CVD processes on the CVD  $W_t/W$  plates used in this study. The theoretical growth rate is further explained in [11].

plate ID	pressure [mbar]	estim. fiber temperature <sup>1</sup> [K]	heater temperature [K]	est. mean partial H <sub>2</sub> pressure [mbar]	theoretical growth rate [nm/s]	meas. thickness of grown CVD plate [μm]	calc. thickness of grown CVD plate [μm]	duration of deposition [h]	H <sub>2</sub> gas exposure before deposition [min]
a	113	771	781	67.9	32.1	1156	1154	10	14
b	125	783	827	73.0	39.7	1223	1248	8.7	15
c	128	767	804	74.7	31.7	1101	1095	9.6	2
d	127	759	804	74.1	28.0	930	936	9.3	1
e	113	764	805	66.0	28.5	970	973	9.5	14

<sup>1</sup> The fiber temperature is estimated by considering the measured thickness of the grown CVD plate and the deposition time. Using the rate equation discussed in [11].

**Table 2**

Characteristics of the samples discussed in this article.

sample name <sup>2</sup>	plate ID	fiber configuration	fiber depth [μm]	wire	oxide interface	fiber/surface ratio	fiber distance [μm]	fiber spacing [μm]
1-Wref								
1a-CVD	a	pure-CVD		pure W (removed)	Er <sub>2</sub> O <sub>3</sub> (removed)		250	100
1a-b/-Er	a	buried (tilted)	35–175	pure W	Er <sub>2</sub> O <sub>3</sub>		250	100
1a-h-Er	a	half-cut		pure W	Er <sub>2</sub> O <sub>3</sub>	40.9%	250	100
1a-t/h-Er	a	touched/half-cut		pure W	Er <sub>2</sub> O <sub>3</sub>	18.5%	250	100
1b-h/-ni	b	half-cut (tilted)		pure W		39.5%	250	100
1b-b-ni	b	buried	60–80	pure W			250	100
1b-t/h-ni	b	touched/half-cut		pure W		20.5%	250	100
2-Wref								
2c-t-Er	c	touched	5–10	pure W	Er <sub>2</sub> O <sub>3</sub>		500	350
2c-b-Er	c	buried	60–70	pure W	Er <sub>2</sub> O <sub>3</sub>		500	350
2d-t-ni	d	touched	5–10	K(60 ppm)			500	350
2d-h-ni	d	half-cut		K(60 ppm)		26.5%	500	350
2e-h/-ni	e	half-cut (tilted)		K(60 ppm)		43.2%	250	100

“Plate ID” refers to the CVD process parameters used for each sample as listed in Table 1. The fiber depth denotes the distance of the fibers to the surface. Whether the fibers are doped with potassium (K) is listed under “wire”. Whether the fibers are coated with an oxide interface is denoted in the column “oxide interface”. In the last three columns, the measured fiber-to-surface ratio, fiber-to-fiber distance and the resulting fiber spacing are denoted.

<sup>2</sup> The sample name consists of the batch number (first or second plasma exposure), the plate ID, the fiber configuration and the interface type. The fiber configuration is denoted by -h- (half-cut), -t- (touched) and -b- (buried). A tilt of the surface with respect to the fiber plane is denoted by “/”. The endings “ni” (no oxide interface) and “Er” (erbium oxide interface) give the interface type.

measured by surface-sensitive methods like NRA. The fiber-surface fraction is very sensitive to the levelness of the fibers and to the orientation of the polishing plane. A sample with a fiber-to-fiber distance of 250 μm can theoretically reach a fiber-surface fraction of 60% while samples with fiber-to-fiber distance of 500 μm can achieve a maximum of 30% fiber-surface fraction. The measured fiber-surface fractions are shown in Table 2 at the column “fiber/surface fraction”.

The exemplary image of the microstructure of “half-cut” samples shows very fine, elongated grains in the fibers (within the yellow boxes) and, in between the fibers, tungsten matrix grains growing with increasing distance to the fibers. Especially towards the middle, where the two growing matrices coincided, the grains have conical shapes (originating from columnar growth on the cylindrical fibers). At the center, an abundance of pores are located which will also be referred to as “pore line”, marked by green arrows.

b) The “**touched**” configuration aims for fibers just below the surface in order to study the impact of an oxide interface compared to a pure tungsten interface on the retention. Differences in the tungsten matrix close to the fibers could also be revealed. The volume of interface in the near-surface region is increased in comparison to the interface volume of “half-cut” samples: In an idealized case, the volume of a 1 μm thick interface is roughly six times larger in a “touched” configuration than for a “half-cut” configuration in the first 7.5 μm depth reachable by NRA.

The exemplary image of a “touched” sample’s microstructure presents similar variation in grain size and shape as the tungsten matrix in the “half-cut”. At the center, pores similar to the pores of the “half-cut” sample but smaller in size are located and marked by

green arrows. At the lateral positions of the fibers, the grain structure of the tungsten matrix – which is lying several microns above the fiber – shows relatively small grains.

c) The purpose of this configuration is the observation of D retention in the matrix at a distance to the fibers where its structure is still influenced by them. Fibers in a “**buried**” configuration are kept deep below the surface, at least several tens of microns. The depth is not reachable by NRA measurements such that the matrix is the only contributor to the H inventory in the near-surface area.

The exemplary microstructure of the “buried” sample has a very similar microstructure to the “touched” sample but shows a far smaller spectrum of grain size and shape: As seen on the “touched” sample, there are smaller grains above the fibers, larger grains between the fibers and pores noticeable at the center. The conical shaped grains which are observed on “half-cut” and “touched” samples are not visible here. In general, the mean grain size is larger compared to the “touched” and the “half-cut” sample.

d) For the “**pure-CVD**” configuration, the fibers were completely removed by grinding. The resulting surface of the remaining matrix was located roughly 200 μm below the fibers. The focus of studying this configuration is to determine the retention of the matrix with a large distance to the fibers. The possible influence of the fibers on the matrix and the H retention is eliminated as far as possible.

The microstructure of the “pure-CVD” sample shows homogeneous and isotropic grains regarding the lateral distribution. No dependence of grain size or shape on the location of the fibers is noticeable. The mean grain size is larger compared to all other samples. There are no visible pores on the surface.

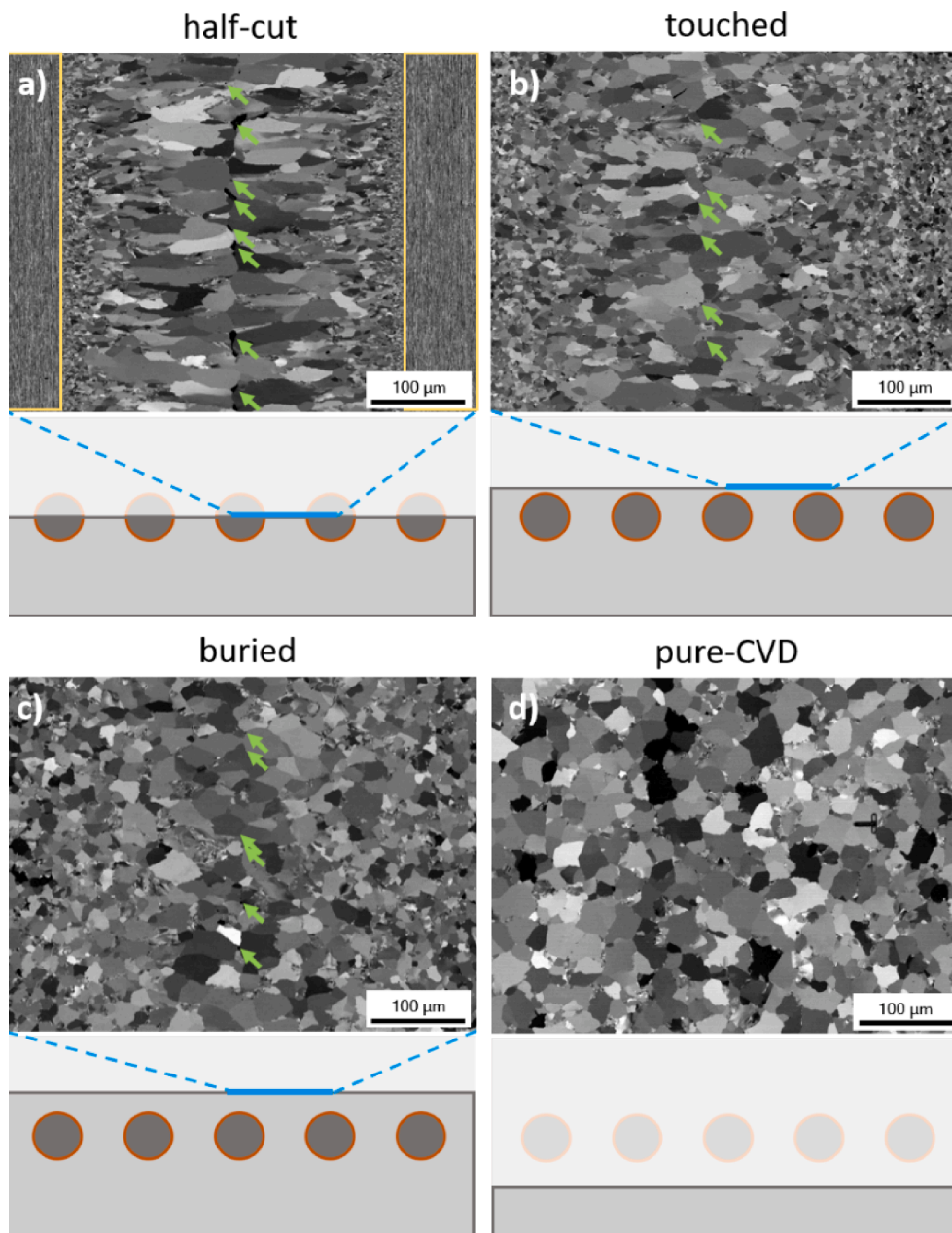


Fig. 2. Schematic drawings of the four fiber configurations used for the study paired with BSE images above showing the microstructure of the upper surface. In the schematic drawings, the light grey bulk is the tungsten matrix, the dark grey circles are the fibers and the red line is the fiber–matrix interface. The faded area is the removed part of the  $W_f/W$  model system. The light blue lines indicate the approximate position regarding the fibers where the microstructural images have been taken. This position is unknown for the configuration “pure-CVD” (d). The yellow rectangles in (a) indicate the location of the fibers and green arrows (a, b, c) point to open pores. Further details can be found in the text.

The fiber configurations are achieved by subsequent grinding and polishing using SiC abrasive paper up to P4000 and a  $1\ \mu\text{m}$  diamond suspension. For a mirror finish, the samples are treated with electrochemical polishing for 30 min using an electrolyte mixture of sodium hydroxide, glycerol and water. In Table 2, the specific characteristics of all samples presented in this article are shown.

As all samples were ground manually and sustaining an even abrasion over a depth of around 1 mm was difficult, for some samples the surface plane and fiber plane are not aligned. These samples are denoted as “tilted” in Table 2. Tilted samples showing fibers on one side of the surface have abrupt changes in microstructure, which has to be treated carefully when evaluating the measurements later on.

### 3. Experimental procedure

The study of D retention in the  $W_f/W$  samples has been carried out in two series (denoted batch 1 and batch 2), following the same experimental procedure.

The samples are annealed in vacuum for 2 h at 900 K. The temperature is chosen such that it is close to the manufacturing temperature (between 780 and 826 K) and neither the potassium-doped nor the pure tungsten wires experience grain growth. Such grain growth has been observed at temperatures as low as 1170 K and an annealing time of 1 h for pure tungsten wires [15]. This effort is made to preserve the characteristic microstructure of the fibers and the comparability of the pure tungsten and K doped wires.

#### 3.1. Plasma exposure

After three weeks of storage in a vacuum desiccator, the samples of one batch are simultaneously placed in the plasma device ‘PlaQ’ which is described in [17]. The D plasma exposure took place at a temperature of 370 K. A bias voltage of  $-10\ \text{V}$  was applied to the sample holder, resulting in a mean implantation energy of  $8.3\ \text{eV/D}$  for the primarily  $D_3^+$  ions. The low implantation energy was chosen to minimize blistering [19]. After plasma exposure with the flux of  $7 \times 10^{19}\ \text{D}/(\text{m}^2\text{s})$  for 72 h, a

fluence of  $2 \times 10^{25}$  D/m<sup>2</sup> was accumulated. Between the two batches, a technical update of the device may have resulted in differences of flux and therefore fluence. The variation is estimated to be below 15%.

### 3.2. Microscopy

Using scanning electron microscopy (SEM) imaging, the microstructure of all samples was characterized and checked for modifications before and after each experimental step with potential influence on the structure. The microscope (Helios NanoLab600, FEI) allows secondary electron (SE) and backscattered electron (BSE) imaging and is equipped with a Ga<sup>+</sup> focused ion beam (FIB). In addition, the surface morphology was examined using a confocal laser scanning microscope (CLSM). The used CLSM (LEXT OLS4000, Olympus) also allows differential interference contrast microscopy (DIC).

## 4. D retention measurements

### 4.1. Nuclear reaction analysis (NRA)

The D in the tungsten samples is probed with a <sup>3</sup>He ion beam at the 3 MV tandem accelerator available at IPP Garching.

For determination of the D concentration depth profiles – referred to as NRA depth profiles, the nuclear reaction <sup>3</sup>He(D, p)<sup>4</sup>He is utilized. The energies of the <sup>3</sup>He beam were chosen to be 690 keV, 800 keV, 1200 keV, 2400 keV, 3200 keV, 3800 keV and 4500 keV. Depending on the energy, the nuclear reaction preferentially takes place at different depths: With 690 keV, the D concentration in the first micron is measured and the highest used energy, 4500 keV, reaches a maximum depth of about 7.5 μm.

The measurements were taken with a square-shaped <sup>3</sup>He beam with the dimensions of roughly 2 by 2 mm in the center of each 10 by 10 mm sample, as is shown on Fig. 3 (a). The resulting proton spectra for each energy are recorded by two proton detectors at a scattering angle of 135° and analyzed using the reaction cross section found in [20]. The depth profiles are obtained by using the NRADC program [21] on the basis of the SIMNRA software [22].

The uncertainties relevant for the comparison between NRA measurements are given by the NRADC program and are below 1%. In order to compare TDS measurements and NRA measurements, the following systematic uncertainties are considered: The uncertainty of the cross-section (4.1 to 5.2%), of the current measurement (3%) and the detector solid angle (3.6 to 3.9%).

NRA can also be used for the investigation of the lateral distribution of the D concentration along the surface of a material, which are referred to as NRA line scans here. For this effort, one single <sup>3</sup>He<sup>+</sup> beam energy of 2400 keV was used, which probes the sample to a depth of 3 μm. During NRA depth profiling of the D concentration, it was found that the highest number of counts was typically obtained around this beam energy, leading to the largest possible sensitivity.

To resolve the potential D concentration fluctuations caused by the unidirectional fibers in the CVD W<sub>f</sub>/W material, the ion beam was narrowed by an aperture to form a line-shaped beam of minimum width and maximum height. Since narrowing the beam strongly reduced the

achievable beam current onto the sample, we chose to make a line-shaped profile. By this, we maximized the beam current and kept the acquisition times for each position of the lateral scan manageable. At the same time, a high lateral resolution was maintained by orienting the unidirectional fibers in our samples parallel to the beam elongation. This geometry of the line scan is depicted in Fig. 3 (b) for the example of a “half-cut” sample: the red rectangular shape marks the beams position in respect to the sample and fiber orientation. The beam is moved along the sample’s surface in the direction of the red arrow.

The exact beam profile was evaluated by image analysis of a burn mark produced on scale paper (Fig. 4a). Averaging the amount of darkening caused by the ion beam over the entire height of the image (the fibers to be measured were aligned parallel to the vertical direction in Fig. 4 (a) resulted in a nearly Gaussian-shaped effective beam profile (Fig. 4 (b)). Depending on the color channels used for analysis, Gaussian fits to the profile yielded a full width at half maximum (FWHM) between 85 and 95 μm. We therefore state the ion beam FWHM as  $90 \pm 5$  μm. The effective length of the line-shaped beam is about 2.3 mm according to Fig. 4 (a).

As an additional test of the lateral resolution that could be obtained under realistic conditions by the method described above, a 2400 keV <sup>3</sup>He beam was scanned across a tungsten fiber fabric with a fiber-to-fiber distance of 300 μm (Fig. 4 (c)). For the evaluation, we integrated the Rutherford backscattering spectroscopy (RBS) signal recorded with a detector at 165° scattering angle in the laboratory system within an energy interval close to the high-energy RBS edge for tungsten. The interval is chosen such that the RBS signal of the sample holder (steel) does not contribute. The beam was scanned across the fibers in intervals of 0.05 mm. The RBS signal shows clearly distinguishable fibers, leading to the conclusion that the method is well suited to determine lateral differences in D retention across the microstructure regions of the W<sub>f</sub>/W samples dedicated for NRA line scans (fiber-to-fiber distance of 500 μm). The same RBS method was used to accurately localize the edge of the W<sub>f</sub>/W samples during NRA line scans (see also Fig. 7 (a, b)).

### 4.2. Thermal desorption spectroscopy (TDS)

The TDS measurement of the W<sub>f</sub>/W composites was conducted with the thermal desorption spectroscopy setup described in [23].

The samples are placed inside a quartz glass tube that is evacuated to 10<sup>-6</sup> Pa. Using an external tubular oven, they are heated with a linear temperature ramp of 3 K/min up to about 1300 K. At least, when this temperature is reached, all D is expected to be released according to previous studies on hot-rolled tungsten [19]. The desorbed gaseous species are monitored by a quadrupole mass spectrometer (Balzers DMM422).

In order to gain the time dependent D desorption flux, the individual D fluxes from the signals of the molecules D<sub>2</sub> and HD are determined using the corresponding calibration factor and summed up (minding the double input from D<sub>2</sub>).

The possible error of the D inventory is dominated by  $\sqrt{N}$ , with N being the number of signal counts. The molecules HD, D<sub>2</sub>, HDO and D<sub>2</sub>O are estimated to be the main contributors to the total D count. The signals of heavy water molecules (HDO and D<sub>2</sub>O) could not be exactly

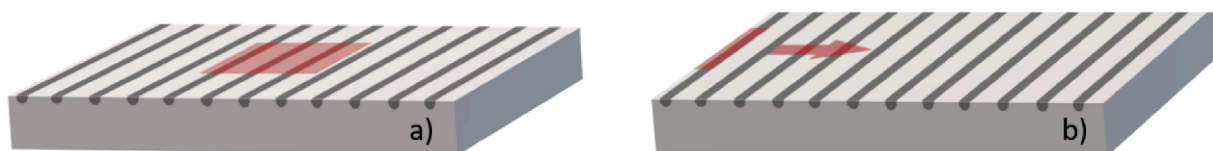
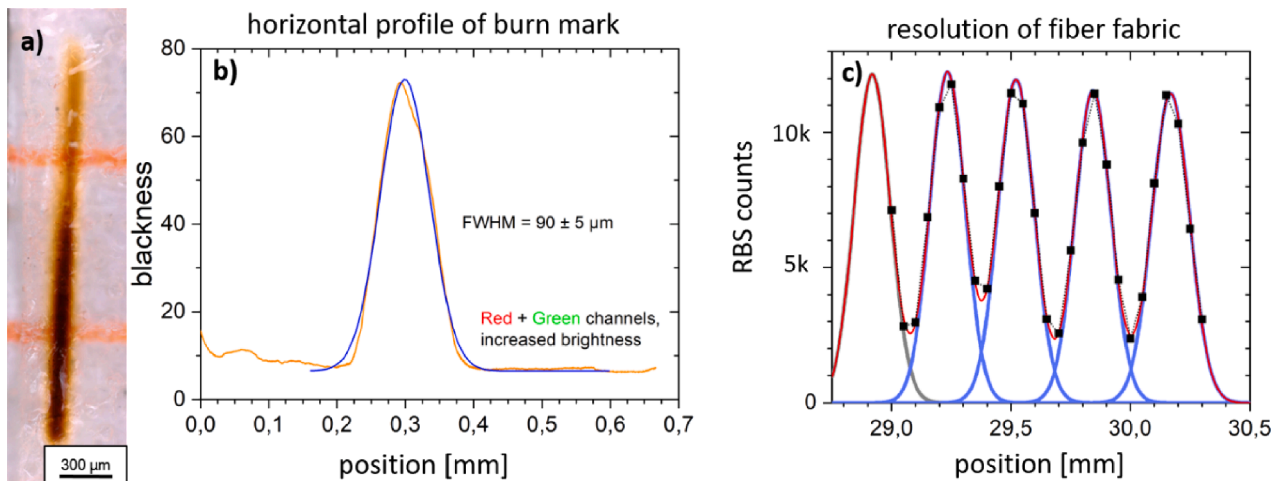


Fig. 3. Schematic depiction of the ion beam position (red rectangle) on the surface of the samples during measurements (a) for NRA depth profiles and (b) for NRA line scans. While the position on the surface is static for the depth profiling, the narrower beam used for the line scans is moved across the sample surface (illustrated by the red arrow).



**Fig. 4.** Image (a) shows the burn mark of the beam spot adjusted for NRA line scans on scale paper. In (b), the horizontal intensity profile of the beam spot averaged over the height of image (a) is given. For a more convenient representation, the darkening is shown instead of the brightness. The blue line corresponds to a Gaussian fit of the peak, from which the FWHM is calculated. Image (c) shows the RBS counts (black squares) of a tungsten fiber fabric with a fiber-to-fiber distance of 300  $\mu\text{m}$  acquired with the narrowed beam spot. The signal is fitted with a superposition of five Gaussian peaks (red line). Blue lines represent the individual peak components.

calibrated due to the lack of an available calibration method for those molecules. Under the assumption that the mass spectrometer sensitivity relation from  $\text{H}_2$  and  $\text{H}_2\text{O}$  is similar to  $\text{D}_2$  and  $\text{D}_2\text{O}$  as well as HD and HDO, the sensitivity factors are taken from literature [24] and used to adjust the calibration. In addition to the uncertainty of calibration, HDO and  $\text{D}_2\text{O}$  from previous measurements adsorbed at the vessel's walls may desorb when heated and fluorine contamination in part of the samples of batch 1 interfered with the heavy water signals. Therefore, the potential contribution of HDO and  $\text{D}_2\text{O}$  to the D inventory is not added to the total value but reflected in the upper error bars of all samples.

## 5. Results and discussion

### 5.1. Microstructure and surface morphology after plasma exposure

The microstructure of the samples before and directly after exposure to D plasma shows no differences when observed with SEM microscopy, as seen in Fig. 5: The grains in both the reference sample (Fig. 5 (a, d)) and the  $W_f/W$  sample (Fig. 5 (b, c, e, f)) shown here give no indication of microstructural changes, as expected for the parameters of the exposure. The grey scale gradient within the grains indicating strains is

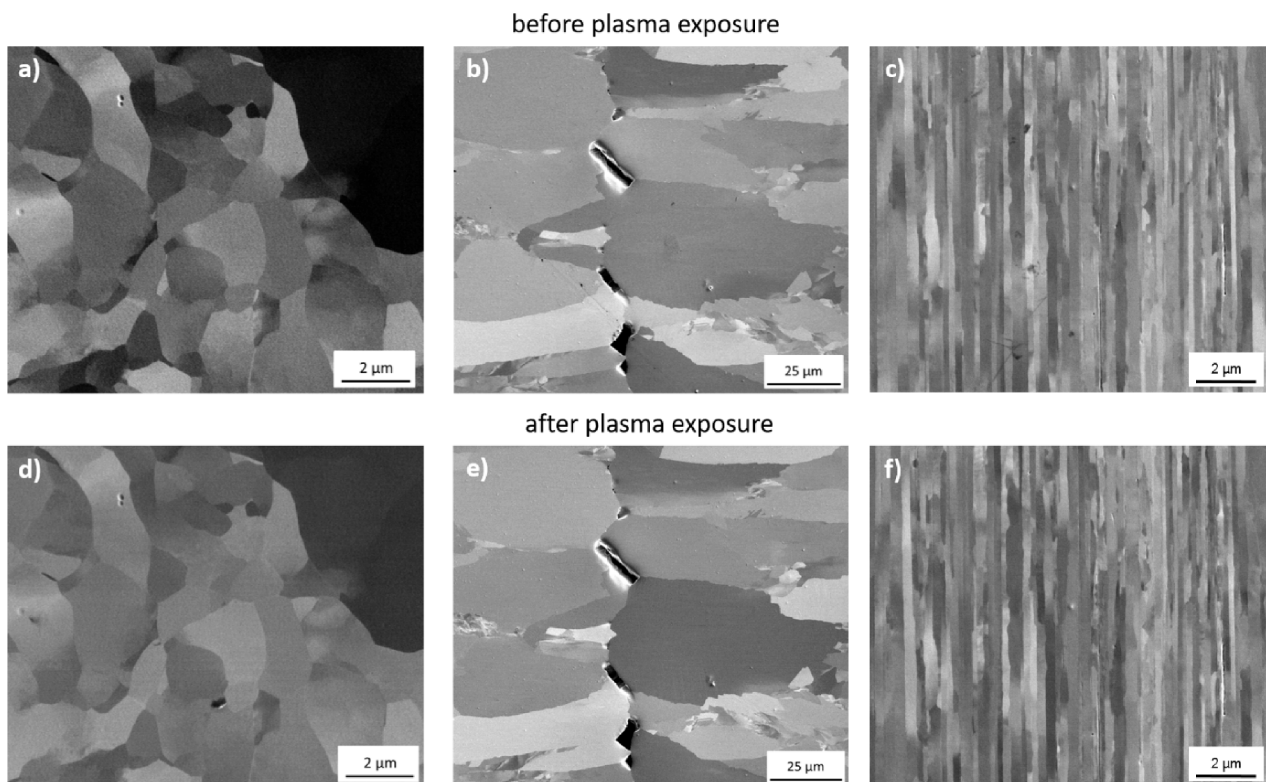


**Fig. 5.** SE images of the microstructure of the reference (a, d) and  $W_f/W$  (b, c, e, f) material. Images (b) and (e) show the microstructure of the tungsten CVD matrix and pores and images (c) and (f) show the microstructure of a tungsten fiber. The upper images (a, b, c) were taken before and the lower images (d, e, f) were taken after exposure to D plasma.

qualitatively unchanged. A change of contrast between the grains is observable, which is expected to be caused by small differences in angle during imaging. This is reflected in the SEM images of the surface of all samples.

In order to detect surface changes, that are on a larger length scale but too shallow to be effectively detected by SEM imaging, the confocal laser scanning microscope (CLSM) is used. The surface topography after plasma exposure is noticeably changed: Both reference samples show a blistering behavior typical for the given parameters of plasma exposure [19] as seen in Fig. 6 (a). For the CVD  $W_f/W$  samples, the only noticeable blisters are observed on fibers that are exposed on the surface as seen in Fig. 6 (b) marked by red circles. The CVD matrix of the composites doesn't show any blisters.

All samples have been examined by CLSM after plasma exposure and blisters are found on all CVD  $W_f/W$  composites with exposed fibers on the surface. Using focused ion beam (FIB) cuts at the location of the observed blisters, cavities in the material below the perceived blister are found as shown in Fig. 6 (c). All probed blisters show such cavities a few micrometers below the surface.

The occurrence of blisters during plasma exposure has previously been linked to higher D retention in hot-rolled tungsten [19,25]. In accordance to this, samples with fibers on the surface might have enhanced D retention.

## 5.2. NRA lateral scans

Two samples with a spacing of 350  $\mu\text{m}$  between the fibers were examined: A "half-cut" sample was chosen in order to observe the differences in retention between fibers and the surrounding tungsten matrix. A NRA line scan of a "buried" sample is supposed to gain information about differences in retention within the tungsten matrix. For precise orientation and matching of the structure in the sample and the signals, both measurements were taken at the edges of the samples. The integrated Rutherford backscattering (RBS) signal at the typical energy range of signal for tungsten is used to accurately determine the position of the edge of the sample. After measurement, pictures of the respective areas on the samples were taken using optical microscopy and measured out to align them closely with the data of the line scans. The graphs with the underlying pictures can be seen in Fig. 7. The areas within the green dotted lines are marking the pore lines on the samples. The blue boxes on the image 7 (a) indicate the position of the fibers on the surface.

The edge of the sample is matched to the position where the RBS signal is half of its maximum value. The error of the proton signal is given by  $\sqrt{N}$  with  $N$  being the counts of the signal.

The "half-cut" sample in Fig. 7 (a) shows two peak types of different height: The prominent peaks are observed at the positions of the fibers and the minor peaks are located at the center between the fibers where the pore lines are. The average proton count per measurement is  $530 \pm 44$ , the maxima at the fibers reach  $611 \pm 25$  counts, the local maxima at the pores give  $530 \pm 5$  counts and the local minima at the matrix are at  $490 \pm 15$  counts. The values are given as averages with standard deviation.

The measurement of the "buried" sample (Fig. 7 (b)) shows peaks located only above the pore lines. The fibers are located 60  $\mu\text{m}$  below the surface, and therefore outside the range of the NRA measurements. Thus, the retention is measured purely in the CVD matrix. The average proton count per measurement point is  $470 \pm 70$ , the maxima at the pore lines being at  $580 \pm 28$  and the minima at  $390 \pm 7$ .

From the lateral scans of both  $W_f/W$  samples it becomes apparent that there is higher D retention in the fibers but the differences in retention between matrix and fiber in the surface near area are rather small. Within the matrix of the "buried" sample, the area of the pore lines contains the most D when looking at the first few  $\mu\text{m}$ . A possible explanation for the high D retention around the pore lines might be a

higher defect concentration at the area where during the CVD process the growing matrices have coincided and formed closed pores, which are afterwards filled with D gas. Since the minima of the NRA proton signals are at areas in the CVD matrix with small grain size, a possible explanation of the lower D retention there in the surface-near area could be an enhanced transport of D in deeper areas. The CVD tungsten matrix and its microstructure around the fibers undeniably plays a substantial role in the hydrogen retention of  $W_f/W$  components.

## 5.3. D retention from NRA and TDS measurements

The D concentration depth profiles from NRA measurements (left) and the D desorption spectra from TDS (right) of a selection<sup>1</sup> of  $W_f/W$  samples and one reference sample are shown in Fig. 8. In general, there are large differences in concentration profile shapes and TDS spectra between the  $W_f/W$  samples themselves, depending on fiber configuration, CVD production parameters, oxide interface and K doping of fibers. The D concentration profile of the reference sample (grey) is typical for hot-rolled tungsten containing blisters on the surface [19]: At the surface and in larger depths, the concentration levels are relatively low while the D concentration is highest at the depth of 1 to 3  $\mu\text{m}$ . This peak can be attributed to the D retained at and around the blisters. The  $W_f/W$  samples generally have higher D concentrations at the near-surface area than the reference tungsten. Depending on the fiber configuration, the D concentrations at the depth of 5 to 7  $\mu\text{m}$  are substantially (i.e. "half-cut") or slightly (i.e. "touched" and "buried") higher for the  $W_f/W$  samples than for the reference sample. In the intermediate depth range, the D concentration is very similar between all samples.

The desorption spectra of the  $W_f/W$  samples show higher desorption fluxes for almost all temperatures in comparison to the reference sample. The "half-cut" samples (orange, red) show a large peak at about 600 K while the "touched" and "buried" samples have plateaus at low temperatures. At temperatures above 800 K the desorption flux seems to be less dependent on the fiber configuration and the differences between the  $W_f/W$  samples are smaller. While the D desorption of the reference sample drastically drops to a very low flux at 800 K and ends at 1000 K, the desorption flux of all  $W_f/W$  is maintained up to 1200 K.

Comparing the depth profiles and the TDS curves of CVD  $W_f/W$  samples with the reference tungsten in Fig. 8, the decisive difference is the higher D concentration that must be located at larger depths.

The large differences in TDS curves at temperatures over 800 K between  $W_f/W$  samples and the reference sample (Fig. 8 (b)) might also be explained by D diffusion from larger depths but could be just as well explained by higher de-trapping energies or slowed down diffusion through re-trapping.

### 5.3.1. Surface-near D inventory from NRA depth profiles

In order to obtain the total inventory of D in the surface-near area (the first 7.5  $\mu\text{m}$ ), the acquired D depth profile functions from the NRA measurements have been integrated. The values for all samples are displayed by the light blue bars in Fig. 9.

On average, the CVD  $W_f/W$  composites have slightly higher near-surface D inventory values than the reference tungsten, as can be seen in Fig. 9. The CVD  $W_f/W$  samples with the lowest D inventories are the "touched" samples – both in batch 1 and batch 2, which have roughly the same values as the reference tungsten. The "touched" sample 1a-t/h-Er represents an exception to that rule.

In the first batch, the samples containing the highest D inventory in the near-surface area are all produced from the same plate "a" but have different fiber configurations: the "half-cut" (1a-h-Er), "buried" (1a-b/-Er) and "pure-CVD" (1a-CVD). The only sample of this plate

<sup>1</sup> The selection of samples shows a variety of NRA and TDS data, but does not show the entirety of occurring D concentration depths profiles and D desorption spectra.

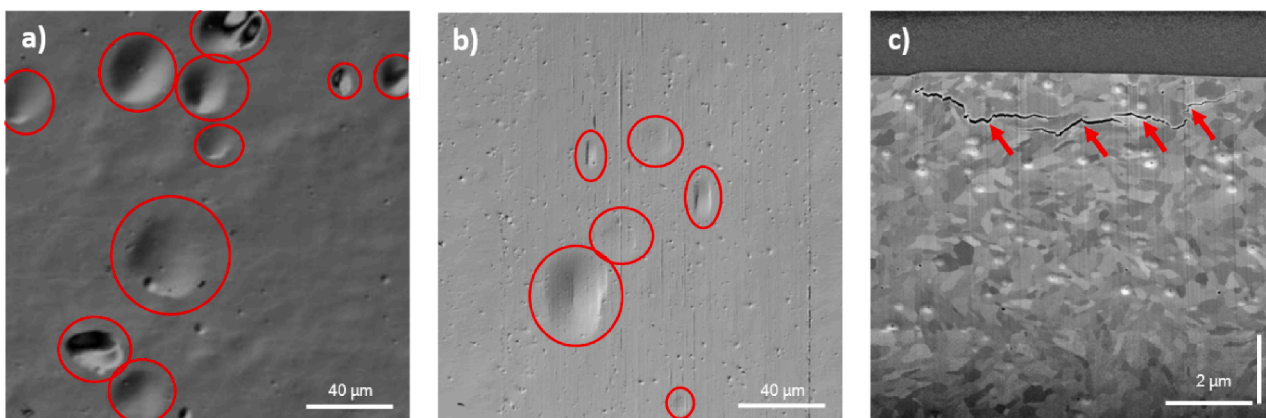


**Fig. 6.** CLSM images using DIC show blisters emerged after plasma exposure on the surface of a reference tungsten sample (a) and a “half-cut”  $W_t/W$  sample (2e-h/-ni) (b). Red circles mark the position of a selection of best noticeable blisters. The perceived light source in images (a) and (b) is located at the bottom right. In (c), red arrows mark the cavities below the surface at the location of a blister on the sample 2e-h/-ni revealed by a FIB cut. The vertical axis of image (c) is tilted by  $-38^\circ$ , which compresses the image in that direction.

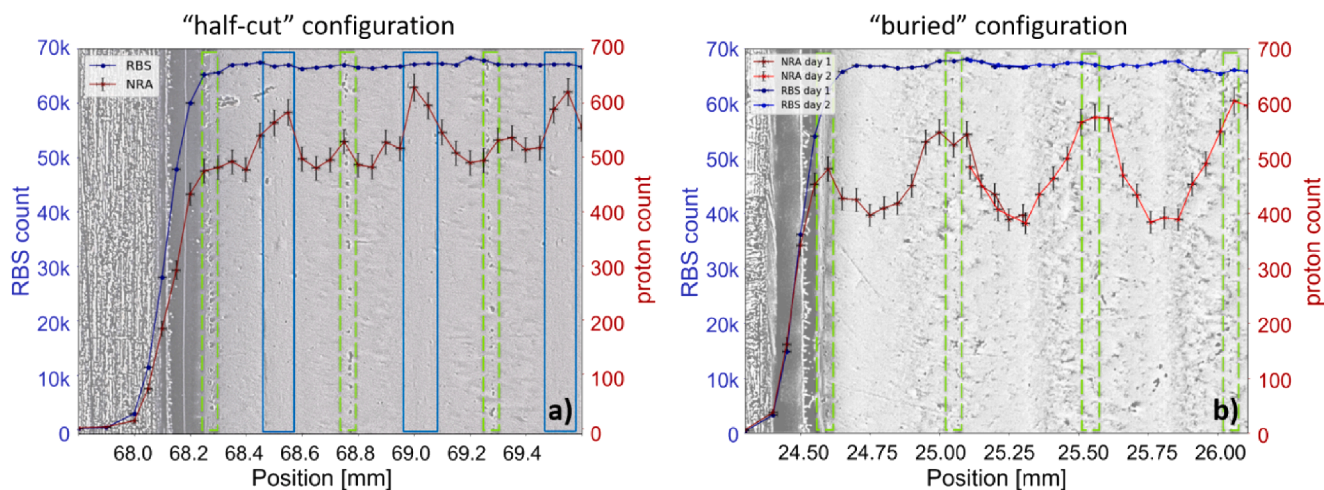


**Fig. 7.** Micro-graphs and results of the RBS and NRA line scan on the “half-cut” sample 2b-h-ni (a) and the “buried” sample 2a-b-Er (b). The red lines mark the proton counts which provides a qualitative distribution of D in the material and the blue lines show the RBS counts used to precisely find the edge of the sample. The x-axis shows the position along the sample. Green dashed rectangles mark the pore lines and blue boxes indicate the fibers. The samples’ edges are at the positions 68.13 mm (a) and 24.50 mm (b), respectively.

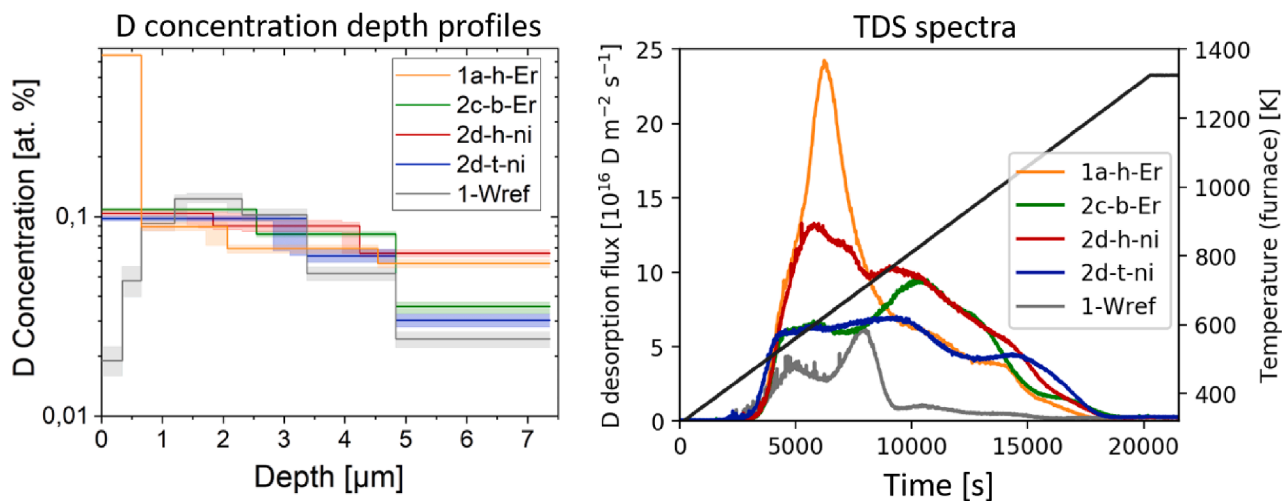


**Fig. 8.** D concentration depth profiles (left), TDS spectra of D desorption flux from  $D_2$  and HD signals (for more details see section 5.3.2) against time (right) of two “half-cut” (1a-h-Er, orange and 2d-h-ni, red), a “touched” (2d-t-ni, blue), a “buried” (2c-b-ni, green) and reference sample (2-Wref, grey).

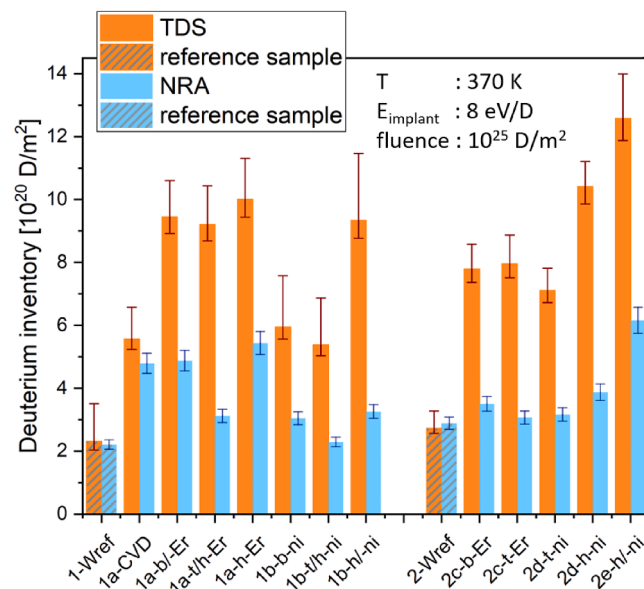


**Fig. 9.** D inventories obtained from NRA depth profiles (light blue) and TDS spectra (orange) of all CVD  $W_f/W$  samples in the study including one reference tungsten sample for each batch (grey striped). The sample name consists of the batch number (first or second plasma exposure), the plate ID, the fiber configuration and the interface type. The fiber configuration is denoted by -h- (half-cut), -t- (touched) and -b- (buried). A tilt of the surface with respect to the fiber plane is denoted by “/”. The endings “ni” (no oxide interface) and “Er” (erbium oxide interface) indicate the interface type.

containing significantly less D is the “touched” sample (1a-t/h-Er). All three samples of the plate “b” are among the lowest D inventories in the near-surface area. The inventory values of the “buried” (1b-b-ni) and the “half-cut” (1b-h/-ni) samples are about 30% higher than the value of the “touched” (1b-t/h-ni) sample.

In the second batch, by far the highest D inventory is found in a “half-cut” sample (2e-h/-ni) which – due to a small spacing (100  $\mu\text{m}$ ) between the fibers – has the highest fiber-surface fraction (43%). The other “half-cut” sample (2d-h-ni) has a fiber-surface fraction of around 26% due to a wider fiber-to-fiber spacing (350  $\mu\text{m}$ ). Its near-surface D inventory is only slightly higher than the D inventory of the reference material and the “touched” samples and roughly the same as the one of the “buried” (2c-b-Er) sample.

The depth profiles from samples with a tilted fiber plane, especially the two “touched” samples from batch 1 (1a-t/h-Er and 1b-t/h-ni), might not be perfectly representative of the whole sample as the microstructure and thereby potentially the H retention is changing throughout the surface area. The area that was used for the NRA depth profiling could not be exactly determined. Since the microstructure on the two “tilted touched” samples doesn’t change purely gradually (due to the fibers), it is possible that the retention behavior (especially when fibers are at the surface) also changes abruptly throughout the samples surface.

Overall, two of the four “half-cut” samples have D retention in the near-surface volume that is more than 10% higher compared to the reference tungsten. Within the error margin, both the “pure-CVD” and “buried” sample of the plate “a” have the same retention values as the high-retaining “half-cuts”. All other samples have just minor (below and around 10%) higher retention compared to the reference.

### 5.3.2. Total D inventory from $D_2$ and HD signals

The total amount of retained D is calculated by integrating the signal peaks of the molecules  $D_2$  and HD over the time. The results are displayed in Fig. 9 as orange bars.

The total D inventories of the reference samples of both batches agree within the estimated uncertainties.

In batch 1, the  $W_f/W$  samples with the lowest D retention are the “pure-CVD” sample 1a-CVD, the “touched/half-cut” sample 1b-t/h-ni and the “buried” sample 1b-b-ni. Nevertheless, they have more than

twice the D retention of the tungsten reference sample. The sample with the highest D inventory is the “half-cut” sample 1a-h-Er, closely followed by the “buried” sample 1a-b/-Er, another “half-cut” sample 1b-h/-ni and a “touched” sample. The differences in D retention between those four samples are smaller than the error margin.

In batch 2, the sample with the highest retention is the “half-cut” sample 2e-h/-ni, followed by the second “half-cut” sample 2d-h-ni. Despite the differences regarding the fiber-matrix interface, the three remaining samples from batch 2 – two “touched” and one “buried” sample – have the same D inventory within the error margins, which is 2.5 to 3 times higher than the D retention of the reference sample.

When comparing the two batches the 2e-h/-ni emerges as the sample with the highest D retention. When normalized to the retention of the respective reference samples, it agrees with the highest retaining four samples of batch 1 within the error margin. The lowest retention is found in the “touched” sample 1b-t/h-ni, which agrees with the 5 other low-retaining samples of both batches (the 1a-CVD and 1b-b-ni and all “touched” and “buried” samples of batch 2) within the error margin.

Overall, besides the high retention in “half-cut” samples, the analysis of the TDS data does not reveal a clear trend explaining the D retention of one  $W_f/W$  sample in relation to the other  $W_f/W$  samples without contradiction.

### 5.3.3. Comparison of NRA and TDS results

As the total D retention measured by TDS has significantly higher values than the D retention in the first 7.5  $\mu\text{m}$  gained by NRA measurements for most  $W_f/W$  samples, the surplus D must be located in deeper regions. For the reference tungsten samples, TDS and NRA values are roughly the same, indicating most of the D remained in the surface-near area. One  $W_f/W$  sample stands out, when comparing the relative NRA and TDS measurements: The “pure-CVD” sample 1a-CVD has only a difference in value around 15% between NRA and TDS measurements.

An explanation for the differences in relation from near-surface to total retention gives an enhanced diffusion of D in most  $W_f/W$  samples compared to the hot-rolled reference tungsten. Since movement along grain boundaries enhances the transport of D [26,27], the microstructure of the samples has large influence here. Non-recrystallized tungsten grains are predominantly oriented along the surface (rolling direction) in the hot-rolled reference sample while the grain boundaries of CVD

$W_f/W$  tungsten are predominantly pointing into the surface due to the columnar growth on the fibers. In contrast, the matrix on the surface of “half-cut” samples has laterally oriented grains. Here, in spite of their laterally oriented grains the exposed fibers are likely to enhance the transport inward along grain boundaries. Due to their very fine microstructure (for a comparison to the microstructure of the reference tungsten, see Fig. 5 (a,c)), there is a large abundance of grain boundaries and there are short, direct paths into the material. The “pure-CVD” sample has quite large grains, which decreases the transport along grain boundaries compared to the other  $W_f/W$  samples. The higher TDS retention values for CVD  $W_f/W$  tungsten composites can therefore be attributed both to a higher D concentration within the near-surface volume and a faster transport into larger depths of the material.

#### 5.4. Comparison to other advanced tungsten materials

$W_f/W$  composites are not the only modified tungsten materials intended for improved performance in plasma-facing components. In order to give a broader perspective to the retention behavior of this composite material, its hydrogen retention is compared to three other tungsten-based materials. As the conditions such as fluence, temperature during implantation and preparation of these samples are often not the same, the D retention in the advanced tungsten materials in relation their reference tungsten material (retention factor) will be compared. Details about the exposure parameters and the D retention are listed in Table 3.

The **tungsten heavy alloy** is a composite material produced by liquid phase sintering. Maier et al. [28] have studied the hydrogen retention of the material with the composition of two weight percent nickel and one weight percent iron which is commercially available. At the fluence of  $10^{25}$  D/m<sup>2</sup>, which is best suited for the comparison to this study, the D retention in the alloy is lower than the retention of the reference material – the retention factor is roughly 0.6.

The **self-passivating tungsten alloy** consisting of tungsten with 10 wt% chromium and 0.5 wt% yttrium is designed to form a stable oxide layer when exposed to oxygen preventing further oxidation and therefore prevent the further formation of radioactive WO<sub>3</sub> [28].

At the fluence of  $10^{25}$  D/m<sup>2</sup> the amount of retained D in the self-passivating alloy surpasses the reference sample by a factor of 8 and only 17% of the D inventory is found in the first 12 μm via NRA measurements.

The D retention of **W/Ta alloys** that contain 1% Ta was compared to reference tungsten in [29]. At a fluence of  $10^{25}$  D/m<sup>2</sup> the alloys surpass the retention of the reference material by a factor of 5 while failing to mitigate the brittleness problem of tungsten. 30% of the D in the tungsten alloys is retained in the first 7.5 μm.

The D retention of CVD  $W_f/W$  is in the middle span regarding the tungsten based materials considered here. It has higher retention than the tungsten heavy alloy but retains less D than the self-passivating and W/Ta alloys.

Concerning the diffusion into the material, the self-passivating tungsten alloy has the least amount of D in the surface near area, even though the NRA measurement reached deeper into the material, meaning that the D transport into the material is strongly enhanced. With a D inventory of 30% in the first 7.5 μm, the W/Ta alloy is close to

the  $W_f/W$  range: Most of the  $W_f/W$  samples have between 35 and 50% D stored in the near surface volume – so the D transport into the material might be slower in the mean, which is favorable.

## 6. Conclusion

The total D retention of the  $W_f/W$  model system samples is higher by factors between 2 and 5 than of the reference tungsten samples. In the production of  $W_f/W$  model system samples, a number of parameters have been varied: Fibers, potassium doping in fibers, surface fraction of fibers, erbium oxide coating on the fibers and various states of microstructure in the CVD matrix. While none of these parameters' influences can be perfectly isolated, some conclusions can be drawn:

1. No parameter has sufficient impact to increase the D retention in the  $W_f/W$  samples by an order of magnitude. The erbium oxide interface and the potassium doping in the fibers, which were suspected to have a significant role regarding the D retention in  $W_f/W$ , did not prove themselves as prominent factors. Even the combination of multiple parameters potentially increasing D retention such as an erbium oxide interface and exposed fibers do not increase the D retention more than by the factor of 5.
2. Especially fibers on the surface, dependent on the fiber-surface fraction, seem to have a larger influence on the total hydrogen retention. Their high degree of deformation, the large abundance of grain boundaries (enhancement of D transport) and their blistering behavior when exposed to D plasma are the plausible causes for that.
3. The retention of  $W_f/W$  samples within the surface-near volume is merely enhanced by a factor of 2 while the total D retention is enhanced by a maximum factor of 5 compared to the reference sample. Thus, obviously enhanced D transport plays a significant role in the total D retention of  $W_f/W$ . The contribution of D transport to the higher total D retention is minimized if the CVD matrix of the sample is at such a large distance (around 200 μm) to the fiber plane that the microstructure is no longer influenced by the fibers and the grains are significantly larger.

Using NRA line scans with specific model systems, a higher D retention in W fibers compared to the surrounding CVD-W matrix has been observed. This is reflected in a higher total D retention of “half-cut” samples compared to most of the samples with other fiber configurations. A significant modulation of D retention within CVD matrix can be seen in the NRA line scans as well as differences in retention between samples of different plates that contain CVD matrices subjected to different production parameters. By optimization of the CVD process, the retention in  $W_f/W$  might be reduced further as the D concentration depth profile of a CVD plate grown on a flat steel surface in [30] suggests.

Since under the inevitable neutron irradiation in the fusion environment, the D retention of conventional plasma-facing tungsten materials increases at least by one order of magnitude [31,32], increase of the D retention through the introduction of  $W_f/W$  composites can be considered less impactful. Indeed, it has already been shown that the initial tungsten grade has very little influence on the D retention in the radiation-damaged state [33]. Whether the retention differences

**Table 3**

Plasma exposure parameters and D retention in tungsten heavy alloy [28], self-passivating alloy [28], W/Ta alloy [29] and CVD  $W_f/W$ .

material	tungsten heavy alloy	self-passivating tungsten alloy	W/Ta alloy	$W_f/W$
annealing	1200 K for 1 h	1200 K for 1 h	1200 K for 12 h	900 K
temperature of plasma exposure	370 K	370 K	330 K	370 K
Implantation energy	38 eV/D	38 eV/D	1 keV/D	8.3 eV/D
D fluence	$10^{25}$ D/m <sup>2</sup>	$10^{25}$ D/m <sup>2</sup>	$10^{24}$ D/m <sup>2</sup>	$10^{25}$ D/m <sup>2</sup>
retention factor	0.6	8	5	2 to 5
near-surface D inventory	–	17% within first 12 μm	30% within first 7.5 μm	33–85% within first 7.5 μm

between  $W_f/W$  and hot-rolled tungsten remain the same after neutron irradiation is the next consequential question to study.

### CRedit authorship contribution statement

**A. Kärcher:** Data curation, Formal analysis, Investigation, Visualization, Writing - original draft. **J. Riesch:** Conceptualization, Data curation, Formal analysis, Methodology, Project administration, Supervision, Validation, Writing - original draft. **P. Almanstötter:** Formal analysis, Investigation. **A. Manhard:** Investigation, Methodology, Validation, Writing - review & editing. **M. Balden:** Data curation, Investigation, Visualization, Writing - review & editing. **J.W. Coenen:** Resources, Writing - review & editing. **K. Hunger:** Data curation, Investigation, Visualization. **H. Maier:** Software, Validation, Writing - review & editing. **L. Raumann:** Resources. **D. Schwalenberg:** Resources. **R. Neu:** Conceptualization, Funding acquisition, Methodology, Supervision, Validation, Writing - review & editing.

### Declaration of Competing Interest

The authors declare that they have no known competing financial interests or personal relationships that could have appeared to influence the work reported in this paper.

### Acknowledgements

This work has been carried out within the framework of the EURO-fusion Consortium and has received funding from the Euratom research and training programme 2014-2018 and 2019-2020 under grant agreement No 633053. The views and opinions expressed herein do not necessarily reflect those of the European Commission.

### References

- W. Espe, M. Knoll, Hochschmelzende Metalle und Legierungen, in: W. Espe, M. Knoll (Eds.), *Werkst. Hochvakuumtechnik Eig. Verarb. Verwend. Werkst. Für Hochvakuumröhren Gasgefüllte Entladungsgefäße*, Springer, Berlin, Heidelberg, 1936: pp. 9–41. [10.1007/978-3-662-24701-3\\_3](https://doi.org/10.1007/978-3-662-24701-3_3).
- V. Philipps, Tungsten as material for plasma-facing components in fusion devices, *J. Nucl. Mater.* 415 (2011) S2–S9, <https://doi.org/10.1016/j.jnucmat.2011.01.110>.
- R. Frauenfelder, Solution and Diffusion of Hydrogen in Tungsten, *J. Vac. Sci. Technol.* 6 (3) (1969) 388–397, <https://doi.org/10.1116/1.1492699>.
- H. Ullmaier, F. Carsughi, Radiation damage problems in high power spallation neutron sources, *Nucl. Instrum. Methods Phys. Res. Sect. B Beam Interact. Mater. At.* 101 (4) (1995) 406–421, [https://doi.org/10.1016/0168-583X\(95\)00590-0](https://doi.org/10.1016/0168-583X(95)00590-0).
- J. Riesch, Entwicklung und Charakterisierung eines wolframfaserverstärkten Wolfram-Verbundwerkstoffs, *Technische Universität München* (2012).
- P. Schade, 100years of doped tungsten wire, *Int. J. Refract. Met. Hard Mater.* 28 (6) (2010) 648–660, <https://doi.org/10.1016/j.ijrmhm.2010.05.003>.
- Y. Mao, J.W. Coenen, J. Riesch, S. Sistla, J. Almanstötter, B. Jasper, A. Terra, T. Hoeschen, H. Gietl, M. Bram, J. Gonzalez-Julian, C. Linsmeier, C. Broeckmann, Development and characterization of powder metallurgically produced discontinuous tungsten fiber reinforced tungsten composites, *Phys. Scr.* T170 (2017), 014005, <https://doi.org/10.1088/0031-8949/2017/T170/014005>.
- Y. Mao, J.W. Coenen, J. Riesch, S. Sistla, C. Chen, Y. Wu, L. Raumann, R. Neu, C. Linsmeier, C. Broeckmann, Spark Plasma Sintering Produced W-Fiber-Reinforced Tungsten Composites, in: P. Cavaliere (Ed.), *Spark Plasma Sinter. Mater. Adv. Process. Appl.*, Springer International Publishing, Cham, 2019: pp. 239–261. [10.1007/978-3-030-05327-7\\_9](https://doi.org/10.1007/978-3-030-05327-7_9).
- J. Riesch, M. Aumann, J.W. Coenen, H. Gietl, G. Holzner, T. Hoeschen, P. Huber, M. Li, C.h. Linsmeier, R. Neu, Chemically deposited tungsten fibre-reinforced tungsten – The way to a mock-up for divertor applications, *Nucl. Mater. Energy.* 9 (2016) 75–83, <https://doi.org/10.1016/j.nme.2016.03.005>.
- H. Gietl, Weiterentwicklung von wolframfaserverstärktem Wolframverbundwerkstoff für den Einsatz in der Fusion, *Technische Universität München* (2018).
- L. Raumann, J.W. Coenen, J. Riesch, Y. Mao, H. Gietl, T. Hoeschen, C.h. Linsmeier, O. Guillon, Modeling and validation of chemical vapor deposition of tungsten for tungsten fiber reinforced tungsten composites, *Surf. Coat. Technol.* 381 (2020), 124745, <https://doi.org/10.1016/j.surfcoat.2019.06.065>.
- J. Riesch, J.-Y. Buffiere, T. Hoeschen, M. di Michiel, M. Scheel, C.h. Linsmeier, J.-H. You, In situ synchrotron tomography estimation of toughening effect by semi-ductile fibre reinforcement in a tungsten-fibre-reinforced tungsten composite system, *Acta Mater.* 61 (19) (2013) 7060–7071, <https://doi.org/10.1016/j.actamat.2013.07.035>.
- J. Riesch, J.-Y. Buffiere, T. Hoeschen, M. Scheel, C.h. Linsmeier, J.-H. You, Crack bridging in as-fabricated and embrittled tungsten single fibre-reinforced tungsten composites shown by a novel in-situ high energy synchrotron tomography bending test, *Nucl. Mater. Energy.* 15 (2018) 1–12, <https://doi.org/10.1016/j.nme.2018.03.007>.
- J. Du, A Feasibility Study of Tungsten-Fiber-Reinforced Tungsten Composites with Engineered Interfaces, *Technische Universität München* (2011).
- V. Nikolić, J. Riesch, R. Pippa, The effect of heat treatments on pure and potassium doped drawn tungsten wires: Part I - Microstructural characterization, *Mater. Sci. Eng. A.* 737 (2018) 422–433, <https://doi.org/10.1016/j.msea.2018.09.027>.
- A. Manhard, M. Balden, S. Elgeti, Quantitative Microstructure and Defect Density Analysis of Polycrystalline Tungsten Reference Samples after Different Heat Treatments, *Pract. Metallogr.* 52 (2015) 437–466, <https://doi.org/10.3139/147.110354>.
- A. Manhard, T. Schwarz-Selinger, W. Jacob, Quantification of the deuterium ion fluxes from a plasma source, *Plasma Sources Sci. Technol.* 20 (2011), 015010, <https://doi.org/10.1088/0963-0252/20/1/015010>.
- C. Linsmeier, M. Rieth, J. Aktaa, T. Chikada, A. Hoffmann, J. Hoffmann, A. Houben, H. Kurishita, X. Jin, M. Li, A. Litnovsky, S. Matsuo, A. von Müller, V. Nikolic, T. Palacios, R. Pippa, D. Qu, J. Reiser, J. Riesch, T. Shikama, R. Stieglitz, T. Weber, S. Wurster, J.-H. You, Z. Zhou, Development of advanced high heat flux and plasma-facing materials, *Nucl. Fusion.* 57 (2017), 092007, <https://doi.org/10.1088/1741-4326/aa6f71>.
- A. Manhard, Deuterium Inventory in Tungsten After Plasma Exposure: A Microstructural Survey, *Universität Augsburg* (2011).
- B. Wielunska, M. Mayer, T. Schwarz-Selinger, U. von Toussaint, J. Bauer, Cross section data for the D(3 He, p) 4 He nuclear reaction from 0.25 to 6 MeV, *Nucl. Instrum. Methods Phys. Res. Sect. B Beam Interact. Mater. At.* 371 (2016) 41–45, <https://doi.org/10.1016/j.nimb.2015.09.049>.
- K. Schmid, U. von Toussaint, Statistically sound evaluation of trace element depth profiles by ion beam analysis, *Nucl. Instrum. Methods Phys. Res. Sect. B Beam Interact. Mater. At.* 281 (2012) 64–71, <https://doi.org/10.1016/j.nimb.2012.03.024>.
- M. Mayer, SIMNRA, a simulation program for the analysis of NRA, RBS and ERDA, *AIP Conf. Proc.* 475 (1999) 541–544, <https://doi.org/10.1063/1.59188>.
- E. Salançon, T. Dürbeck, T. Schwarz-Selinger, F. Genoeise, W. Jacob, Redeposition of amorphous hydrogenated carbon films during thermal decomposition, *J. Nucl. Mater.* 376 (2) (2008) 160–168, <https://doi.org/10.1016/j.jnucmat.2008.02.070>.
- Hidden Analytical, Relative Sensitivity: RS Measurements of Gases, (n.d.). [https://www.hidden.de/wp-content/uploads/pdf/RS\\_Measurement\\_of\\_Gases\\_-\\_Hidden\\_Analytical\\_App\\_Note\\_282.pdf](https://www.hidden.de/wp-content/uploads/pdf/RS_Measurement_of_Gases_-_Hidden_Analytical_App_Note_282.pdf) (accessed July 27, 2020).
- A. Manhard, L. Gao, Blisters formed by D plasma exposure in an electron-transparent tungsten sample, *Nucl. Mater. Energy.* 17 (2018) 248–252, <https://doi.org/10.1016/j.nme.2018.11.014>.
- M. Pecovnik, S. Markelj, A. Založnik, T. Schwarz-Selinger, Influence of grain size on deuterium transport and retention in self-damaged tungsten, *J. Nucl. Mater.* 513 (2019) 198–208, <https://doi.org/10.1016/j.jnucmat.2018.10.026>.
- U. von Toussaint, S. Gori, A. Manhard, T. Hoeschen, C. Hoeschen, Molecular dynamics study of grain boundary diffusion of hydrogen in tungsten, *Phys. Scr.* T145 (2011), 014036, <https://doi.org/10.1088/0031-8949/2011/T145/014036>.
- H. Maier, T. Schwarz-Selinger, R. Neu, C. Garcia-Rosales, M. Balden, A. Calvo, T. Dürbeck, A. Manhard, N. Ordás, T.F. Silva, Deuterium retention in tungsten based materials for fusion applications, *Nucl. Mater. Energy.* 18 (2019) 245–249, <https://doi.org/10.1016/j.nme.2018.12.032>.
- K. Schmid, V. Rieger, A. Manhard, Comparison of hydrogen retention in W and V/Ta alloys, *J. Nucl. Mater.* 426 (1-3) (2012) 247–253, <https://doi.org/10.1016/j.jnucmat.2012.04.003>.
- J.W. Coenen, M. Berger, M.J. Demkowicz, D. Matveev, A. Manhard, R. Neu, J. Riesch, B. Unterberg, M. Wirtz, C.h. Linsmeier, Plasma-wall interaction of advanced materials, *Nucl. Mater. Energy.* 12 (2017) 307–312, <https://doi.org/10.1016/j.nme.2016.10.008>.
- T. Schwarz-Selinger, J. Bauer, S. Elgeti, S. Markelj, Influence of the presence of deuterium on displacement damage in tungsten, *Nucl. Mater. Energy.* 17 (2018) 228–234, <https://doi.org/10.1016/j.nme.2018.10.005>.
- S. Markelj, O.V. Ogorodnikova, P. Pelicon, T. Schwarz-Selinger, K. Sugiyama, I. Čadež, Study of thermal hydrogen atom interaction with undamaged and self-damaged tungsten, *J. Nucl. Mater.* 438 (2013) S1027–S1031, <https://doi.org/10.1016/j.jnucmat.2013.01.224>.
- O.V. Ogorodnikova, K. Sugiyama, Effect of radiation-induced damage on deuterium retention in tungsten, tungsten coatings and Eurofer, *J. Nucl. Mater.* 442 (1-3) (2013) 518–527, <https://doi.org/10.1016/j.jnucmat.2013.07.024>.